

# Improved corrosion resistance of novel Fe-based amorphous alloys

Jiawei Li <sup>a,b</sup>, Lijing Yang <sup>c</sup>, Haoran Ma <sup>a,b</sup>, Kemin Jiang <sup>d</sup>, Chuntao Chang <sup>a,b,\*</sup>, Jun-Qiang Wang <sup>a,b,\*</sup>, Zhenlun Song <sup>a,b</sup>, Xinmin Wang <sup>a,b</sup>, Run-Wei Li <sup>a,b</sup>

<sup>a</sup> Key Laboratory of Magnetic Materials and Devices, Ningbo Institute of Materials Technology & Engineering, Chinese Academy of Sciences, Ningbo, Zhejiang 315201, China

<sup>b</sup> Zhejiang Province Key Laboratory of Magnetic Materials and Application Technology, Ningbo Institute of Materials Technology & Engineering, Chinese Academy of Sciences, Ningbo, Zhejiang 315201, China

<sup>c</sup> Key Laboratory of Marine Materials and Related Technologies, Zhejiang Key Laboratory of Marine Materials and Protective Technologies, Ningbo Institute of Materials Technology and Engineering, Chinese Academy of Sciences, Ningbo, Zhejiang 315201, China

<sup>d</sup> Center for Analysis and Measurements, Ningbo Institute of Materials Technology & Engineering, Chinese Academy of Sciences, Ningbo, Zhejiang 315201, China

## ARTICLE INFO

### Article history:

Received 12 October 2015

Received in revised form 19 January 2016

Accepted 21 January 2016

Available online 22 January 2016

### Keywords:

Fe-based

Amorphous alloys

Corrosion

XPS

## ABSTRACT

Developing amorphous alloys with good corrosion resistance have attracted wide interests recently. In this work, a series of  $\text{Fe}_{71-x}\text{Cr}_x\text{Mo}_{3.5}\text{Ni}_5\text{P}_{10}\text{C}_4\text{B}_4\text{Si}_{2.5}$  ( $x = 0, 4, 8, 10, 12, 14$  at.%) amorphous alloys are fabricated. Thermal stability of this alloy system increases slightly with appropriate Cr content. The corrosion resistance in 3.5 wt.% NaCl solution is sensitive to the minor addition of Cr ( $\leq 4$  at.%) whereas higher Cr does not significantly improve the corrosion resistance according to the results of electrochemical measurements, SEM and XPS. These Fe-based amorphous alloys show comparable corrosion resistance with the well-known amorphous steel ( $\text{Fe}_{48}\text{Mo}_{14}\text{Cr}_{15}\text{Y}_2\text{C}_{15}\text{B}_6$ ) despite the low Cr and Mo content, making them good candidates as corrosion-resistant coating materials.

## 1. Introduction

Fe-based amorphous alloys, with high corrosion resistance, excellent soft-magnetic and mechanical properties, have drawn extensive attention [1,2]. Recently some of these alloys have been sprayed as protective coatings on numerous prototypes and parts, which show better corrosion and wear resistance than conventional stainless steels and Ni-based materials, sufficient to warrant their use in drilling, refining, shipping, tunnel-boring, etc. [3–6]. Specifically, the Fe-Cr-Mo-C-B system known as amorphous steel received extensive attention due to its high glass-forming ability (GFA) and corrosion resistance in harsh environments [5–22]. The effect of compositional optimization on the corrosion properties of this alloy system has been studied in details. It was found that the additions of Cr [6,9,13], Mo [9,17], W [13], P [10], B [7,15], Y [18], Al [8], Ni [8], Co [8], and N [8] benefit the corrosion resistance of the system. However, all these alloys contain a large amount of Mo ( $\geq 14$  at.%) and Cr ( $\geq 15$  at.%), leading to an increase in materials cost. Recent studies show that minor Cr addition to the amorphous steels results in corrosion resistance comparable with that of Cr-rich alloys, but they unfavorably contain 14 at.% Mo [11]. Therefore, the development

of novel corrosion-resistant Fe-based amorphous alloys with low Mo is of high importance in both basic research and industrial applications. It is known that Ni-P alloy has been widely used in the mechanical and electronic industries due to their excellent corrosion and wear resistance [23]. P is the most effective metalloid element in enhancing the corrosion resistance of Fe-Cr based alloys [24], and Ni shows the best corrosion resistance among the iron group metals [25]. Thus, partial replacement of Mo by P and Ni may decrease the materials cost of amorphous steels without deteriorating the corrosion properties.

In this study, good thermal stability and outstanding corrosion-resistant properties were designed by adding Cr to our recently developed  $\text{Fe}_{71}\text{Mo}_{3.5}\text{Ni}_5\text{P}_{10}\text{C}_4\text{B}_4\text{Si}_{2.5}$  alloy with high GFA (cylinders with up to 5.5 mm in diameter) [26]. The novel  $\text{Fe}_{71-x}\text{Cr}_x\text{Mo}_{3.5}\text{Ni}_5\text{P}_{10}\text{C}_4\text{B}_4\text{Si}_{2.5}$  amorphous alloys exhibit corrosion resistance comparable to the common amorphous steels despite their low Cr and Mo content [15,20]. This work will enlighten further research on designing new amorphous alloys with unique properties.

## 2. Experimental procedure

Master alloys with nominal compositions of  $\text{Fe}_{71-x}\text{Cr}_x\text{Mo}_{3.5}\text{Ni}_5\text{P}_{10}\text{C}_4\text{B}_4\text{Si}_{2.5}$  ( $x = 0, 4, 8, 10, 12, 14$  at.%) were prepared by induction melting the mixtures of pure Fe, Cr, Ni, Mo metals, pure B and Si crystals, and pre-alloyed Fe-P and Fe-C ingots under an argon

\* Corresponding authors at: Key Laboratory of Magnetic Materials and Devices, Ningbo Institute of Materials Technology & Engineering, Chinese Academy of Sciences, Ningbo, Zhejiang 315201, China.

E-mail addresses: ctchang@nimte.ac.cn (C. Chang), jqwang@nimte.ac.cn (J.-Q. Wang).

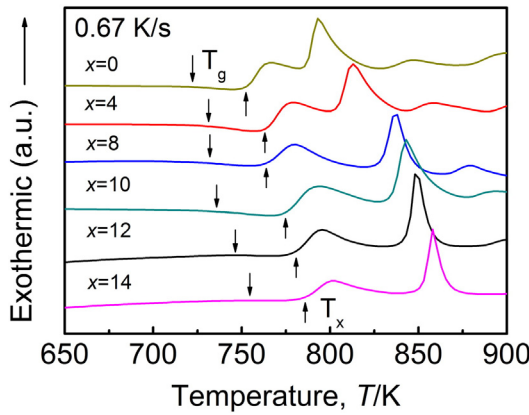


**Fig. 1.** DSC traces of the  $\text{Fe}_{71-x}\text{Cr}_x\text{Mo}_{3.5}\text{Ni}_5\text{P}_{10}\text{C}_4\text{B}_4\text{Si}_{2.5}$  ( $x = 0, 4, 8, 10, 12, 14$  at.%) amorphous ribbons at a heating rate of 0.67 K/s.

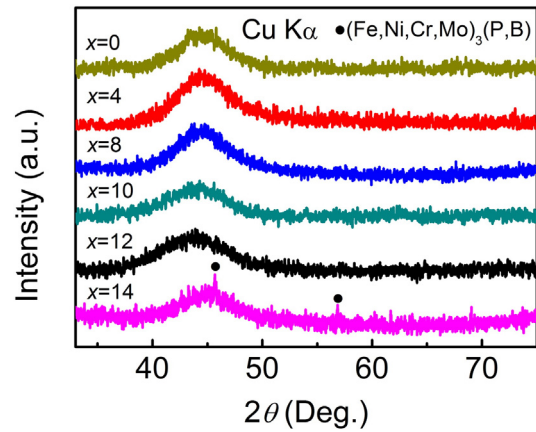


**Fig. 2.** XRD patterns of the  $\text{Fe}_{71-x}\text{Cr}_x\text{Mo}_{3.5}\text{Ni}_5\text{P}_{10}\text{C}_4\text{B}_4\text{Si}_{2.5}$  ( $x = 0, 4, 8, 10, 12, 14$  at.%) amorphous ribbons.

atmosphere. Ribbons with a cross-section of  $1\text{--}1.5 \times 0.03\text{--}0.04 \text{ mm}^2$  were prepared by single roller melt-spinning method in an argon atmosphere at a surface speed of 35 m/s. The amorphous nature of the samples was verified by X-ray diffraction (XRD, Bruker D8 Advance) with Cu K $\alpha$  radiation. The thermal stability of the ribbons was investigated by differential scanning calorimetry (DSC, NETZSCH 404C) at a heating rate of 0.67 K/s. Corrosion resistance measurements were carried out by electrochemical work station (AUTOLAB PGSTAT 302) in aerobic 3.5 wt.% NaCl solution at room temperature. A three-electrode cell was employed, with the samples acting as the working electrode, the saturated calomel electrode (SCE) as the reference electrode, and a platinum sheet as the counter electrode. Prior to electrochemical tests, all samples were polished with metallographic sandpaper of 2000 grain size, washed in ethanol, and dried in air for 24 h. Potentiodynamic polarization curves were measured at a scanning rate of 2 mV/s after immersion of the samples for 20 min when the open-circuit potential became almost steady. Electrochemical impedance spectroscopy (EIS) measurements were performed at open circuit potential and room temperature after a 20 min exposure to the test solution. The EIS method was used in the frequency range from  $10^5$  to 0.01 Hz and involved the perturbation amplitude of 10 mV. All electrochemical measurements were repeated five times for reliability and repeatability. The topography and corrosion products of the amorphous samples after the electrochemical measurements were analyzed by scanning electron microscopy (SEM, FEI Quanta FEG 250) and X-ray photoelectron spectroscopy (XPS, AXIS Ultra DLD) with a monochromatic Al K $\alpha$  X-ray source ( $h\nu = 1486.6$  eV), respectively.

### 3. Results and discussion

Fig. 1 shows the DSC traces of  $\text{Fe}_{71-x}\text{Cr}_x\text{Mo}_{3.5}\text{Ni}_5\text{P}_{10}\text{C}_4\text{B}_4\text{Si}_{2.5}$  ( $x = 0, 4, 8, 10, 12, 14$  at.%) amorphous ribbons at a heating rate of 0.67 K/s. The

thermal parameters associated with glass transition temperature ( $T_g$ ), crystallization temperature ( $T_x$ ) and supercooled liquid region ( $\Delta T_x = T_x - T_g$ ) are summarized in Table 1. Upon heating, both  $T_g$  and  $T_x$  shift towards higher temperatures with the increase in Cr content. The  $\Delta T_x$  value increases from 31 to 39 K with increase in Cr content from 0 to 10, while decreases to 31 K when the Cr content reaches 14. This trend suggests that the highest thermal stability of the present alloy system can be obtained by adding near 10 at.% of Cr, but begins to decrease with further Cr addition [27]. The critical cylindrical diameters for  $x \leq 10$  are larger than or equal to 2 mm. The amorphous nature of the melt-spun ribbons was verified by XRD, as shown in Fig. 2. Apart from the  $x = 14$  alloy, which exhibits a very weak peak corresponding to  $(\text{Fe}, \text{Ni}, \text{Cr}, \text{Mo})_3(\text{B}, \text{P})$  metastable [26,28], all alloys show only a broad diffraction peak without any detectable sharp Bragg peaks, indicating their fully amorphous structure.

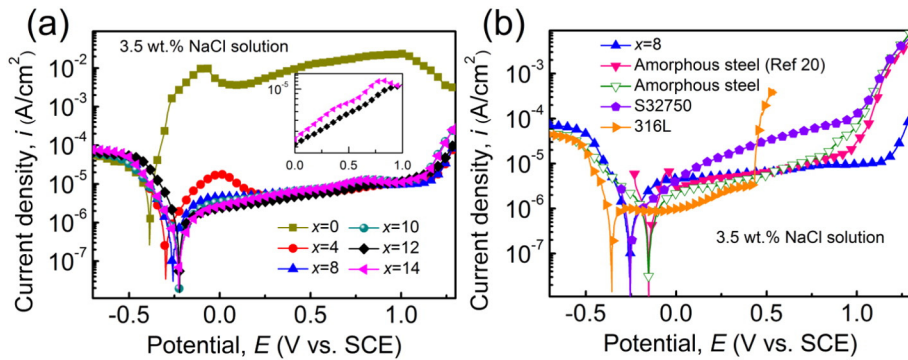
To evaluate the corrosion resistance, electrochemical measurements in 3.5 wt.% NaCl solution at room temperature were performed. Fig. 3(a) shows the representative potentiodynamic polarization curves of  $\text{Fe}_{71-x}\text{Cr}_x\text{Mo}_{3.5}\text{Ni}_5\text{P}_{10}\text{C}_4\text{B}_4\text{Si}_{2.5}$  ( $x = 0, 4, 8, 10, 12, 14$  at.%) amorphous ribbons. The corrosion current density ( $I_{\text{corr}}$ ), passivation current density ( $I_{\text{pass}}$ ) and corrosion potential ( $E_{\text{corr}}$ ) obtained by the Tafel extrapolation method are reported in Table 1. It is observed that all Cr-containing samples exhibit a large passive region until the transpassive dissolution of Cr occurs [12]. In the absence of Cr, the amorphous alloy shows low  $E_{\text{corr}}$  and high  $I_{\text{corr}}$  without exhibiting any passive plateau. However, the alloys with 4 at.% of Cr exhibit a pronounced active/passive transition behavior accompanied by an active dissolution peak. Alloys with more than 8 at.% Cr exhibit similar polarization plots to each other and are spontaneously passivated with a relatively high  $E_{\text{corr}}$ , low  $I_{\text{corr}}$  and  $I_{\text{pass}}$ .

Fig. 3(b) shows the potentiodynamic polarization curves of  $x = 8$  alloy, super duplex stainless steels UNS S32750, austenitic steel AISI

**Table 1**

Thermal and electrochemical parameters obtained from the DSC traces, polarization curves and EIS spectra of  $\text{Fe}_{71-x}\text{Cr}_x\text{Mo}_{3.5}\text{Ni}_5\text{P}_{10}\text{C}_4\text{B}_4\text{Si}_{2.5}$  ( $x = 0, 4, 8, 10, 12, 14$  at.%) amorphous ribbons, respectively.  $T_g$ ,  $T_x$ ,  $\Delta T_x$ ,  $I_{\text{corr}}$ ,  $I_{\text{pass}}$ ,  $E_{\text{corr}}$  and  $R_t$  represent the glass transition temperature, crystallization temperature, supercooled liquid region, corrosion current density, passivation current density, corrosion potential and charge transfer resistance, respectively.

	Thermal parameters			Electrochemical parameters			
	$T_g$ (K)	$T_x$ (K)	$\Delta T_x$ (K)	$I_{\text{corr}}$ ( $\text{A}/\text{cm}^2$ )	$I_{\text{pass}}$ ( $\text{A}/\text{cm}^2$ )	$E_{\text{corr}}$ (V)	$R_t$ ( $\text{k}\Omega \text{ cm}^2$ )
$x = 0$	722	753	31	$6.48 \pm 0.37 \times 10^{-6}$	—	$-0.37 \pm 0.026$	$1.62 \pm 0.52$
$x = 4$	730	763	33	$5.80 \pm 0.44 \times 10^{-7}$	$9.19 \pm 3.48 \times 10^{-6}$	$-0.30 \pm 0.005$	$34.80 \pm 4.32$
$x = 8$	732	765	33	$5.04 \pm 0.36 \times 10^{-7}$	$7.60 \pm 2.82 \times 10^{-6}$	$-0.26 \pm 0.017$	$47.67 \pm 0.54$
$x = 10$	736	775	39	$3.42 \pm 0.11 \times 10^{-7}$	$7.42 \pm 4.23 \times 10^{-6}$	$-0.23 \pm 0.004$	$180.50 \pm 36.50$
$x = 12$	746	781	35	$2.47 \pm 0.24 \times 10^{-7}$	$6.83 \pm 4.67 \times 10^{-6}$	$-0.22 \pm 0.004$	$666.63 \pm 67.01$
$x = 14$	755	786	31	$2.90 \pm 0.28 \times 10^{-7}$	$7.30 \pm 4.96 \times 10^{-6}$	$-0.23 \pm 0.005$	$424.70 \pm 77.70$



**Fig. 3.** Potentiodynamic polarization curves in 3.5 wt.% NaCl solution at room temperature for: (a)  $\text{Fe}_{71-x}\text{Cr}_x\text{Mo}_{3.5}\text{Ni}_5\text{P}_{10}\text{C}_4\text{B}_4\text{Si}_{2.5}$  ( $x = 0, 4, 8, 10, 12, 14$  at.%) amorphous ribbons, (b)  $x = 8$  alloy ( $\text{Fe}_{69.88}\text{Cr}_{8.26}\text{Mo}_{6.67}\text{Ni}_{5.83}\text{P}_{6.15}\text{C}_{0.95}\text{B}_{0.86}\text{Si}_{1.4}$  wt.-%), super duplex stainless steels UNS S32750 ( $\text{Fe}_{62.99}\text{Cr}_{25.15}\text{Mo}_{3.43}\text{Ni}_{6.74}\text{P}_{0.03}\text{C}_{0.02}\text{Si}_{0.55}\text{N}_{0.27}\text{Mn}_{0.69}\text{Cu}_{0.13}$  wt.-%), austenitic steel AISI 316 L ( $\text{Fe}_{55.16}\text{Cr}_{17.54}\text{Mo}_{2.47}\text{Ni}_{12.3}\text{P}_{0.02}\text{C}_{0.03}\text{Si}_{0.44}\text{Mn}_{1.84}$  wt.-%), and amorphous steel ( $\text{Fe}_{51.29}\text{Cr}_{14.92}\text{Mo}_{25.7}\text{C}_{3.45}\text{B}_{1.24}\text{Y}_{3.4}$  wt.-%) obtained from this work and Ref. 20. The chemical compositions are given in mass percent for comparison.

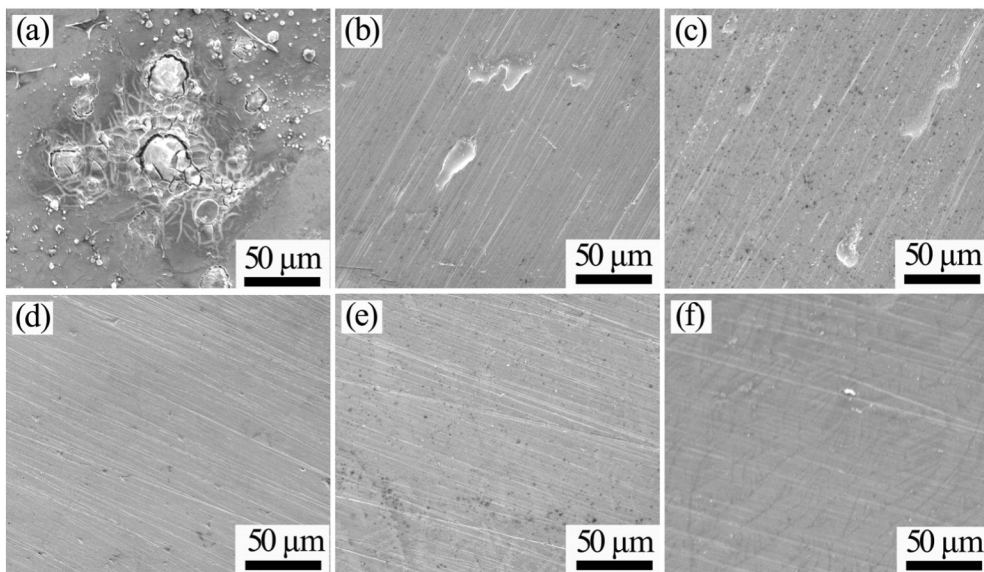
316 L and amorphous steel. The comparison of the polarization curves indicates that all the alloys are spontaneously passivated with a very low  $I_{\text{corr}}$  and  $I_{\text{pass}}$  on the order of  $10^{-7}$  and  $10^{-6}$  A/cm<sup>2</sup> respectively. However, the  $x = 8$  alloy exhibits a more stable and wider passive region than the S32750, 316 L and amorphous steel, implying a superior passive film protection. Thus, the  $x = 8$  alloy with the highest breakdown voltage shows better corrosion resistance than the others. It should be noted that the novel developed Fe-based amorphous alloy has very low Mo, Ni and Cr content. The polarization results provide us a guideline for designing high corrosion-resistant Fe-based amorphous alloys in different corrosive media. For example, adding minor amounts of Ni and P to Fe-Cr-metallloid alloys significantly increases the corrosion resistance of the alloys without deteriorating their GFA despite the very low Cr and Mo content.

As shown in Fig. 3(a) and Table 1, addition of 4 at.% Cr to the Fe–Mo–Ni–P–C–B–Si alloy results in two orders in the  $I_{\text{pass}}$  and one order reduction in the  $I_{\text{corr}}$ , respectively, compared to the Cr-free alloy. However, there is no distinct difference in the electrochemical parameters for the alloys with higher Cr ( $\geq 8$  at.%). Moreover, it is interesting to find that the  $x = 14$  alloy exhibits a bit higher  $I_{\text{pass}}$  than the  $x = 12$  alloy at potentials of 0–1 V (see the inset in Fig. 3). These results indicate that

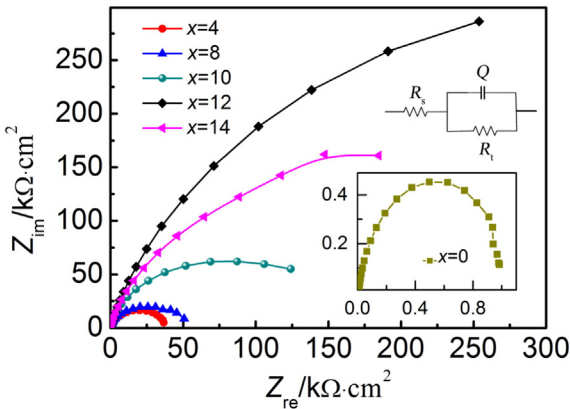
minor addition of Cr is very effective in improving the corrosion resistance of the present alloy system in the chloride-containing environment, whereas more Cr addition does not enhance the corrosion resistance further.

Fig. 4 displays SEM micrographs of the electrochemical corroded surfaces of  $\text{Fe}_{71-x}\text{Cr}_x\text{Mo}_{3.5}\text{Ni}_5\text{P}_{10}\text{C}_4\text{B}_4\text{Si}_{2.5}$  ( $x = 0, 4, 8, 10, 12, 14$  at.%) amorphous ribbons. In Fig. 4(a) the surface of Cr-free alloy is completely damaged and covered by a thick layer of polarized product. In Fig. 4(b) and (c) a small amount of polarized products and tiny pits are evident for the  $x = 4$  and 8 alloys. However, in Fig. 4(d), (e) and (f) the polarized products and pits on the surfaces of  $x = 10, 12$  and 14 alloys are more obscure than the  $x = 4$  and 8 samples, indicating that their corroded surfaces are less damaged. Thereby the SEM micrographs confirm that the amount of pits and corrosion products are dependent of Cr content in a Cl<sup>−</sup> containing media. The EDS results (not shown) indicate that the compositional elements on the films of all samples are consistent with the nominal compositions of  $\text{Fe}_{71-x}\text{Cr}_x\text{Mo}_{3.5}\text{Ni}_5\text{P}_{10}\text{C}_4\text{B}_4\text{Si}_{2.5}$  ( $x = 0, 4, 8, 10, 12, 14$  at.%), but the Cr-free sample contains much more oxygen content in comparison to the samples with Cr.

Fig. 5 shows the Nyquist plots of  $\text{Fe}_{71-x}\text{Cr}_x\text{Mo}_{3.5}\text{Ni}_5\text{P}_{10}\text{C}_4\text{B}_4\text{Si}_{2.5}$  ( $x = 0, 4, 8, 10, 12, 14$  at.%) amorphous ribbons in 3.5 wt.% NaCl solution



**Fig. 4.** SEM micrographs of the electrochemical corroded surfaces of the  $\text{Fe}_{71-x}\text{Cr}_x\text{Mo}_{3.5}\text{Ni}_5\text{P}_{10}\text{C}_4\text{B}_4\text{Si}_{2.5}$  ( $x = 0, 4, 8, 10, 12, 14$  at.%) amorphous ribbons. In (a) the surface of  $x = 0$  alloy is completely damaged. In (b) and (c) the surfaces of  $x = 4$  and 8 alloys are covered by a small amount of corrosion products. In (d), (e) and (f) the surfaces of  $x = 10, 12$  and 14 alloys are less damaged.



**Fig. 5.** Nyquist plots of  $\text{Fe}_{71-x}\text{Cr}_x\text{Mo}_{3.5}\text{Ni}_3\text{P}_{10}\text{C}_4\text{B}_4\text{Si}_{2.5}$  ( $x = 0, 4, 8, 10, 12, 14$  at.%) amorphous ribbons in 3.5 wt.% NaCl solution at room temperature. Insets: (top-right) equivalent circuit describing the electrochemical reaction and (down-right) the curve of  $x = 0$  alloy, showing the smallest semicircle diameter in the Nyquist plots. The equivalent circuit,  $R_s(R_tQ)$ , is used to fit the impedance spectra.

at room temperature. The curve of  $x = 0$  alloy has been inserted into Fig. 5 for clarity. The Nyquist plots of all samples show only one capacitive loop, implying one single time constant in the electrochemical measurement. The semicircle diameter in the Nyquist plots increases remarkably with increasing Cr from  $x = 0$  to 12, but decreases with more Cr addition. This result suggests that the  $x = 12$  alloy has the largest charge transfer resistance among these alloys. To fit the impedance spectra, an appropriate equivalent circuit describing the electrochemical reaction,  $R_s(R_tQ)$ , is shown in the top-right inset of Fig. 5, where  $R_s$  is the solution resistance,  $R_t$  is the charge transfer resistance, and  $Q$  is used to represent the possibility of a non-ideal capacitance. As shown in Table 1, the  $R_t$  increases significantly with minor Cr addition and reaches the highest value at  $x = 12$ . However, with increasing Cr content from  $x = 12$  to 14, the value of  $R_t$  decreases from 666.63 to 424.70  $\text{k}\Omega \cdot \text{cm}^2$ . It is known that the larger the  $R_t$ , the better the corrosion resistance [29]. Thus the EIS data agrees well with the results of electrochemical measurements.

To better understand the effect of Cr addition on the corrosion mechanism, XPS analysis was performed to characterize the chemical composition of oxide films formed on the surfaces of the amorphous ribbons after electrochemical testing in 3.5 wt.% NaCl solution. Fig. 6 illustrates the spectra of Fe 2p and Cr 2p in  $x = 12$  and 14 alloys after Ar-ion sputtering for 55 s. The spectra are normalized to the same height at their maximum peaks and moved up and down as necessary. The Fe 2p spectrums corresponding to the peaks of  $\text{Fe } 2p_{1/2}$  and  $2p_{3/2}$  include

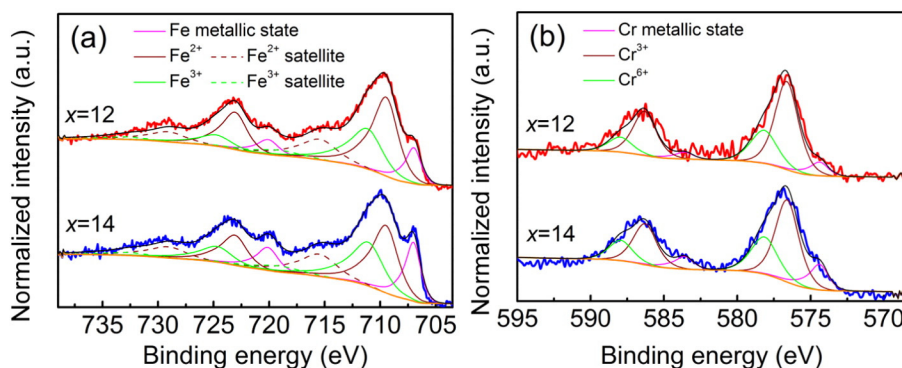
the peaks of the metallic state ( $\text{Fe}^m$ ),  $\text{Fe}^{2+}$  and  $\text{Fe}^{3+}$  oxide states ( $\text{Fe}^{ox}$ ). In addition, two satellite peaks occur at about 8 eV ( $\text{Fe}^{3+}$ ) and 6 eV ( $\text{Fe}^{2+}$ ) higher binding energies than the main Fe 2p peaks [30]. The Cr 2p peaks represent the metallic state ( $\text{Cr}^m$ ),  $\text{Cr}^{3+}$  and  $\text{Cr}^{6+}$  oxide states ( $\text{Cr}^{ox}$ ). As shown in Fig. 6(a), the peak intensity of the  $\text{Fe}^m$  in  $x = 14$  alloy is relatively higher than that of  $x = 12$  alloy. Fig. 6(b) shows that the total area of Cr 2p peaks in  $x = 14$  alloy is larger than that in  $x = 12$  alloy, suggesting a higher concentration of Cr on the surface of  $x = 14$  alloy.

Fig. 7 shows the Fe 2p and Cr 2p XPS depth profile spectra of  $x = 12$  and 14 alloys with Ar-ion sputtering for 15, 55, 115, 235 and 475 s. The spectra are normalized to the same height at their maximum peaks for comparison. The peak positions of Fe and Cr in the oxide films are similar to each other whereas there are some differences between the peak intensities. With the increase in etching time, the peak intensities of the metallic states increase accompanied with the decrease in the corresponding oxides states. In addition, relatively higher  $\text{Fe}^m$  and  $\text{Cr}^m$  peaks are found on the surface of  $x = 14$  alloy during the entire etching process. According to the XPS theory, the thickness of oxide film can be expressed as [31]:

$$I_o/I_s = \rho_o \lambda_o (e^{t \cos \theta / \lambda_o} - 1) / \rho_s \lambda_s$$

where  $I_o$  is the oxide film intensity (count per second, CPS),  $I_s$  is the metal substrate intensity (CPS),  $\rho_o$  is the oxide film density ( $\text{kg}/\text{m}^3$ ),  $\rho_s$  is the metal substrate density ( $\text{kg}/\text{m}^3$ ),  $\lambda_o$  is the oxide film electron inelastic mean free path (IMFP, nm),  $\lambda_s$  is the metal substrate IMFP (nm),  $t$  is the thickness of oxide film (nm) and  $\theta$  is the electron emission angle. It is reasonable to deduce that the larger the ratio of metal oxide to its corresponding metallic state, the thicker the oxide film under the same measurement conditions. Thus, it is necessary to identify the metal oxide/metallic ratio in the oxide film.

Fig. 8 represents the etching time dependence of  $\text{Fe}^{ox}/\text{Fe}^m$  and  $\text{Cr}^{ox}/\text{Cr}^m$  ratios in the oxide films of  $x = 12$  and 14 alloys. The values of  $\text{Fe}^{ox}/\text{Fe}^m$  and  $\text{Cr}^{ox}/\text{Cr}^m$  decrease with the etching time, and then tend to be the same after sputtering for 235 s since the etching depth has almost reached the alloy matrix. It is clearly seen that the oxide ratios of  $x = 12$  alloy are higher than those of  $x = 14$  alloy, indicating that the surface of  $x = 12$  alloy develops a thicker oxide film after the potentiodynamic polarization. On the other hand, the precipitation of  $(\text{Fe}, \text{Ni}, \text{Cr}, \text{Mo})_3(\text{B}, \text{P})$  metastable nanocrystalline phase in the  $x = 14$  alloy may consume a small amount of Cr, which in turn results in the depletion of Cr around the nanocrystalline phase [32], decreasing the thickness of the oxide film. Based on the above results, the formation of a more stable and protective layer on the  $x = 12$  alloy might be responsible for the observed relatively higher corrosion behavior.



**Fig. 6.** XPS spectra of (a) Fe 2p and (b) Cr 2p recorded from the surfaces of  $x = 12$  and 14 alloys after electrochemical corroded in 3.5 wt.% NaCl solution with Ar-ion sputtering for 55 s. In (a) the Fe 2p spectrums correspond to the peaks of Fe metallic,  $\text{Fe}^{2+}$  and  $\text{Fe}^{3+}$  states. The dashed curves show the satellite peaks of  $\text{Fe}^{2+}$  and  $\text{Fe}^{3+}$  states. In (b) the Cr 2p spectrums represent the peaks of Cr metallic,  $\text{Cr}^{3+}$  and  $\text{Cr}^{6+}$  states. The spectra indicate that the total areas of Fe and Cr metallic peaks in  $x = 14$  alloy are relatively higher than those in  $x = 12$  alloy.

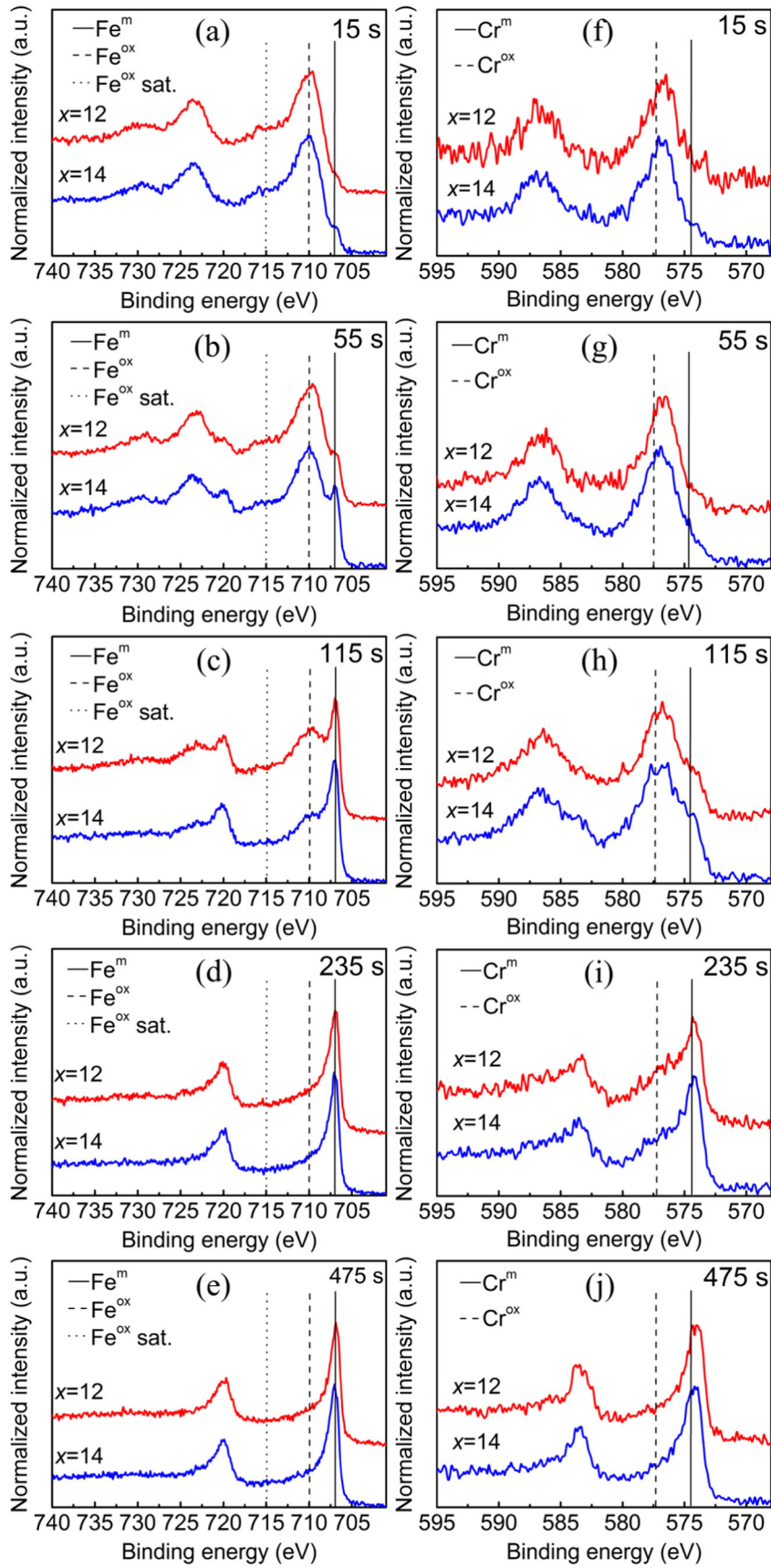


**Fig. 7.** Fe 2p and Cr 2p XPS depth profile spectra of (a–e)  $x = 12$  and (f–j)  $x = 14$  alloys with Ar-ion sputtering for 15, 55, 115, 235 and 475 s, respectively. The main peak positions change gradually to lower binding energies with sputtering time. The intensities of Fe and Cr metallic peaks in  $x = 14$  alloy are relatively higher compared with the  $x = 12$  alloy (superscript m: metallic state; superscript ox: metal oxide state; Sat.: satellite).

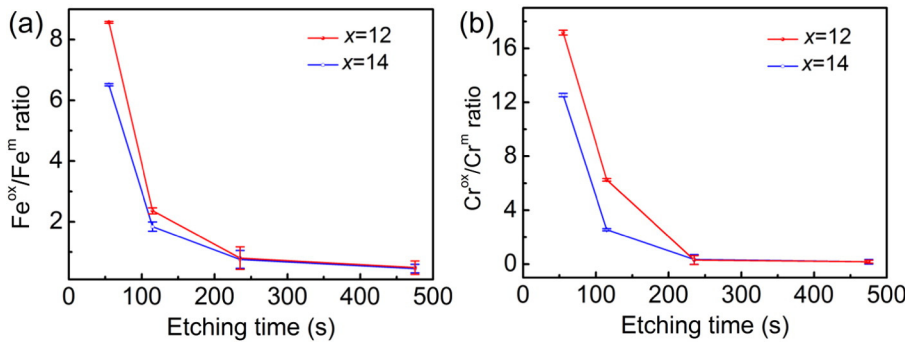


**Fig. 8.** Etching time dependence of (a)  $\text{Fe}^{\text{ox}}/\text{Fe}^{\text{m}}$  and (b)  $\text{Cr}^{\text{ox}}/\text{Cr}^{\text{m}}$  ratios in the oxide films of  $x = 12$  and 14 alloys. The ratios were obtained from the  $\text{Fe}\ 2p$  and  $\text{Cr}\ 2p$  curves fitted by vision processing software. The metal oxide/metallic ratios of  $x = 12$  alloy are higher than those of  $x = 14$  alloy up to 235 s, suggesting the  $x = 12$  alloy might form a thicker oxide film.

#### 4. Conclusions

To reduce the content of Cr and Mo in the well-known amorphous steel, a series of  $\text{Fe}_{71-x}\text{Cr}_x\text{Mo}_{3.5}\text{Ni}_5\text{P}_{10}\text{C}_4\text{B}_4\text{Si}_{2.5}$  ( $x = 0, 4, 8, 10, 12, 14$  at.%) amorphous alloys have been fabricated successfully. Their thermal stability and corrosion resistance were investigated. The results can be summarized as follows:

- (1) The substitution of 4–12 at.% Fe by Cr increases the glass transition temperature of the present alloy system, suggesting their good thermal stability.
- (2) The minor alloying of Cr by 4 at.% can significantly increase the corrosion resistance in 3.5 wt.% NaCl solution. Further Cr addition will increase the corrosion resistance slightly with the best response obtained for the  $x = 12$  alloy, which could be attributed to the formation of thick oxide film. More addition of Cr slightly decreases the thermal stability and corrosion resistance due to the precipitation of  $(\text{Fe}, \text{Ni}, \text{Cr}, \text{Mo})_3(\text{B}, \text{P})$  metastable phase.
- (3) These Fe-based amorphous alloys with a combination of high GFA, excellent corrosion resistance and relatively low Mo and Cr content, are good candidates for applications as corrosion-resistant coating materials.

#### Acknowledgments

This work was supported by National Natural Science Foundation of China (Grant Nos. 51501210 and 51571207) and Ningbo Municipal Nature Science Foundation (Grant Nos. 2015A610002 and 2015A610064). Particular thanks to S.J. Pang, M.X. Zhang and W.M. Yang for their discussions.

#### References

- [1] C. Suryanarayana, A. Inoue, Iron-based bulk metallic glasses, *Int. Mater. Rev.* 58 (2013) 131–166.
- [2] W.M. Yang, H.S. Liu, Y.C. Zhao, A. Inoue, K.M. Jiang, J.T. Huo, H.B. Ling, Q. Li, B.L. Shen, Mechanical properties and structural features of novel Fe-based bulk metallic glasses with unprecedented plasticity, *Sci. Rep.* 4 (2014) 6233.
- [3] E. Axinte, Metallic glasses from “alchemy” to pure science: present and future of design, processing and applications of glassy metals, *Mater. Des.* 35 (2012) 518–556.
- [4] W.M. Guo, J.F. Zhang, Y.P. Wu, S. Hong, Y.J. Qin, Fabrication and characterization of Fe-based amorphous coatings prepared by high-velocity arc spraying, *Mater. Des.* 78 (2015) 118–124.
- [5] W. Wang, C. Zhang, P. Xu, M. Yasir, L. Liu, Enhancement of oxidation and wear resistance of Fe-based amorphous coatings by surface modification of feedstock powders, *Mater. Des.* 73 (2015) 35–41.
- [6] J. Farmer, J.S. Choi, C. Saw, J. Haslam, D. Day, P. Hailey, T.G. Lian, R. Rebak, J. Perepezko, J. Payer, D. Branagan, B. Beardsley, A. D’Amato, L. Aprigliano, Iron-based amorphous metals: high-performance corrosion-resistant material development, *Metall. Mater. Trans. A* 40A (2009) 1289–1305.
- [7] S.J. Pang, T. Zhang, K. Asami, A. Inoue, Bulk glassy Fe–Cr–Mo–C–B alloys with high corrosion resistance, *Corros. Sci.* 44 (2002) 1847–1856.
- [8] J. Jayaraj, Y.C. Kim, K.B. Kim, H.K. Seok, E. Fleury, Corrosion behaviors of  $\text{Fe}_{45-x}\text{Cr}_{18}\text{Mo}_{14}\text{C}_{15}\text{B}_6\text{Y}_2\text{M}_x$  ( $\text{M} = \text{Al, Co, Ni, N}$  and  $x = 0, 2$ ) bulk metallic glasses under conditions simulating fuel cell environment, *J. Alloys Compd.* 434 (2007) 237–239.
- [9] S.J. Pang, T. Zhang, K. Asami, A. Inoue, Formation of bulk glassy  $\text{Fe}_{75-x-y}\text{Cr}_x\text{Mo}_{15}\text{B}_{10}$  alloys and their corrosion behavior, *J. Mater. Res.* 17 (2002) 701–704.
- [10] S.J. Pang, T. Zhang, K. Asami, A. Inoue, Synthesis of Fe–Cr–Mo–C–B–P bulk metallic glasses with high corrosion resistance, *Acta Mater.* 50 (2002) 489–497.
- [11] M. Madinehei, P. Bruna, M.J. Duarte, E. Pineda, J. Klemm, F.U. Renner, Glass-formation and corrosion properties of Fe–Cr–Mo–C–B glassy ribbons with low Cr content, *J. Alloys Compd.* 615 (2014) S128–S131.
- [12] M.J. Duarte, J. Klemm, S.O. Klemm, K.J.J. Mayrhofer, M. Stratmann, S. Borodin, A.H. Romero, M. Madinehei, D. Crespo, J. Serrano, S.S.A. Gerstl, P.P. Choi, D. Raabe, F.U. Renner, Element-resolved corrosion analysis of stainless-type glass-forming steels, *Science* 341 (2013) 372–376.
- [13] T. Xu, S.J. Pang, T. Zhang, Glass formation, corrosion behavior, and mechanical properties of novel Cr-rich Cr–Fe–Mo–C–B–Y bulk metallic glasses, *J. Alloys Compd.* 625 (2015) 318–322.
- [14] F.Q. Zhai, E. Pineda, M.J. Duarte, D. Crespo, Role of Nb in glass formation of Fe–Cr–Mo–C–B–Nb BMGs, *J. Alloys Compd.* 604 (2014) 157–163.
- [15] P.H. Tsai, A.C. Xiao, J.B. Li, J.S.C. Jang, J.P. Chu, J.C. Huang, Prominent Fe-based bulk amorphous steel alloy with large supercooled liquid region and superior corrosion resistance, *J. Alloys Compd.* 586 (2014) 94–98.
- [16] Y.J. Huang, Y.Z. Guo, H.B. Fan, J. Shen, Synthesis of Fe–Cr–Mo–C–B amorphous coating with high corrosion resistance, *Mater. Lett.* 89 (2012) 229–232.
- [17] Q.J. Chen, LL. Hu, X.L. Zhou, X.Z. Hu, Y.J. Yang, Effect of corrosive medium on the corrosion resistance of FeCrMoCB amorphous alloy coating, *Adv. Mater. Res.* 291–294 (2011) 65–71.
- [18] Z.M. Wang, Y.T. Ma, J. Zhang, W.L. Hou, X.C. Chang, J.Q. Wang, Influence of yttrium as a minority alloying element on the corrosion behavior in Fe-based bulk metallic glasses, *Electrochim. Acta* 54 (2008) 261–269.
- [19] V. Ponnambalam, S.J. Poon, G.J. Shiflet, Fe-based bulk metallic glasses with diameter thickness larger than one centimeter, *J. Mater. Res.* 19 (2004) 1320–1323.
- [20] C. Zhang, R.Q. Guo, Y. Yang, Y. Wu, L. Liu, Influence of the size of spraying powders on the microstructure and corrosion resistance of Fe-based amorphous coating, *Electrochim. Acta* 56 (2011) 6380–6388.
- [21] J. Shen, Q.J. Chen, J.F. Sun, H.B. Fan, G. Wang, Exceptionally high glass-forming ability of an FeCoCrMoCBY alloy, *Appl. Phys. Lett.* 88 (2005) 151907.
- [22] P.F. Gostin, S. Oswald, L. Schultz, A. Gebert, Acid corrosion process of Fe-based bulk metallic glass, *Corros. Sci.* 62 (2012) 112–121.
- [23] R.M.A. Hameed, A.M. Fekry, Electrochemical impedance studies of modified Ni–P and Ni–Cu–P deposits in alkaline medium, *Electrochim. Acta* 55 (2010) 5922–5929.
- [24] M. Naka, K. Hashimoto, T. Masumoto, Effect of metalloid elements on corrosion resistance of amorphous iron–chromium alloys, *J. Non-Cryst. Solids* 28 (1978) 403–413.
- [25] Z.L. Long, C.T. Chang, Y.H. Ding, Y. Shao, P. Zhang, B.L. Shen, A. Inoue, Corrosion behavior of Fe-based ferromagnetic (Fe, Ni)–B–Si–Nb bulk glassy alloys in aqueous electrolytes, *J. Non-Cryst. Solids* 354 (2008) 4609–4613.
- [26] M.X. Zhang, A.D. Wang, B.L. Shen, Enhancement of glass-forming ability of Fe-based bulk metallic glasses with high saturation magnetic flux density, *AIP Adv.* 2 (2012) 022169.
- [27] A. Inoue, Stabilization of metallic supercooled liquid and bulk amorphous alloys, *Acta Mater.* 48 (2000) 279–306.
- [28] B.L. Shen, M. Akiba, A. Inoue, Effects of Si and Mo additions on glass-forming in FeGaPCB bulk glassy alloys with high saturation magnetization, *Phys. Rev. B* 73 (2006) 104204.
- [29] A. Kocijan, D.K. Merl, M. Jenko, The corrosion behaviour of austenitic and duplex stainless steels in artificial saliva with the addition of fluoride, *Corros. Sci.* 53 (2011) 776–783.
- [30] T. Yamashita, P. Hayes, Analysis of XPS spectra of  $\text{Fe}^{2+}$  and  $\text{Fe}^{3+}$  ions in oxide materials, *Appl. Surf. Sci.* 254 (2008) 2441–2449.
- [31] J.F. Watts, J. Wolstenholme, *An Introduction To Surface Analysis by XPS and AES*, in, Wiley, Rexdale, 2003 79–111.
- [32] Y. Yang, C. Zhang, Y. Peng, Y. Yu, L. Liu, Effects of crystallization on the corrosion resistance of Fe-based amorphous coatings, *Corros. Sci.* 59 (2012) 10–19.